J. Fluid Mech. (2007), *vol.* 573, *pp.* 211–236.
doi:10.1017/S002211200600379X Printed in the United Kingdom

Impulsive fluid forcing and water strider locomotion

OLIVER BÜHLER

Center for Atmosphere Ocean Science at the Courant Institute of Mathematical Sciences
New York University, New York, NY 10012, USA

(Received 19 September 2005 and in revised form 4 August 2006)

This paper presents a study of the global response of a fluid to impulsive and localized forcing; it has been motivated by the recent laboratory experiments on the locomotion of water-walking insects reported in Hu, Chan & Bush (*Nature*, vol. 424, 2003, p. 663). These insects create both waves and vortices by their rapid leg strokes and it has been a matter of some debate whether either form of motion predominates in the momentum budget. The main result of this paper is to argue that generically both waves and vortices are significant, and that in linear theory they take up the horizontal momentum with share 1/3 and 2/3, respectively.

This generic result, which depends only on the impulsive and localized nature of the forcing, is established using the classical linear impulse theory, with adaptations to weakly compressible flows and flows with a free surface. Additional general comments on experimental techniques for momentum measurement and on the wave emission are given and then the theory is applied in detail to water-walking insects.

Owing to its generality, this kind of result and the methods used to derive it should be applicable to a wider range of wave–vortex problems in the biolocomotion of water-walking animals and elsewhere.

1. Introduction

The aim of this paper is to understand the exchange of momentum between a water-walking insect and the fluid underneath during the insect's rapid leg stroke. The original motivation for this paper stems from the experimental work of Hu, Chan & Bush (2003) on the exchange of horizontal momentum in the special case of the water strider (also known as a pond skater). However, it now appears that the fluid-dynamical issues are relevant for a much broader range of water-walking animals, some of which use the exchange of vertical momentum during leg strokes in a systematic way (e.g. Bush & Hu 2006, and references therein). Thus, both horizontal and vertical momentum exchanges are discussed in this paper.

During the leg stroke there is an equal-and-opposite exchange of momentum between the insect's moving leg and the fluid underneath, and the insect uses the horizontal component of this recoil to propel itself forward. The opposite recoil felt by the fluid generates both surface waves and vortices in the fluid and this leads to the question of whether waves or vortices predominate in their uptake of the recoil momentum. Another question is whether it is possible to suppress either waves or vortices entirely during the leg stroke. The present paper argues that both waves and vortices are inevitable during the leg stroke, and that in linear theory they take up the horizontal recoil momentum with share 1/3 and 2/3, respectively. This means it

is impossible to completely suppress either waves or vortices. This result is generic in the sense that it does not depend on the details of the surface waves (such as whether surface tension is present or not); rather it depends only on the spatially localized and impulsive nature of the momentum exchange.

The fluid-dynamical arguments leading to this generic result are adaptations of classical arguments on fluid momentum and Kelvin's hydrodynamic impulse, which can be found in the incompressible flow theory part of Lamb (1932). However, these arguments appear not to be very widely known, and thus it seems useful to draw the threads together in one place and present these arguments here together with their adaptations to compressible and free-surface flows and with their application to the water strider problem at hand.

The key phenomenon to be understood is the global response of a fluid to a force field that is both impulsive and spatially localized. Depending on the nature of the fluid and its boundary conditions (e.g. depending on its compressibility and on the presence of free or rigid boundaries) the response of the fluid will differ in detail, but it will always involve the propagation of pressure waves (possibly with infinite speed) to large distances away from the forcing site and therefore it will always involve the motion of fluid particles at large distances as well.

Moreover, the fluid motion typically involves both waves and vortices and it is a natural question to ask how the structure of the force field affects the magnitude of the excited waves compared to the excited vortices. As alluded to earlier, it will turn out that in many cases the relative magnitudes of wave and vortex momentum do not depend on the structure of the force field at all, provided only that the force field is impulsive and localized.

The essence of this result can be understood based on a simpler statement, namely that it turns out that the relevant momentum content in the waves and in the vortices is proportional to the first spatial moments of $\nabla \cdot \boldsymbol{F}$ and of $\nabla \times \boldsymbol{F}$, respectively, where $\boldsymbol{F}(\boldsymbol{x})$ is the spatial structure of the impulsive force field. In general there is no link between these first moments but for localized force fields (which vanish outside a finite region of support) there is a trivial integration-by-parts identity

$$\int \boldsymbol{F}\,\mathrm{d}V = -\int \boldsymbol{x}\,\nabla\cdot\boldsymbol{F}\,\mathrm{d}V = \frac{1}{n-1}\int \boldsymbol{x}\times(\nabla\times\boldsymbol{F})\,\mathrm{d}V, \tag{1.1}$$

where n is the number of spatial dimensions and the volume integral is extended over a domain that contains the support of $\boldsymbol{F}$ but is otherwise arbitrary.

The identity (1.1) illustrates clearly that if $n>1$ then a localized vector field must necessarily have both a potential part and a non-divergent vortical part, and that for all values of n the first moments of these parts are matched in the ratio $1/(n-1)$. By implication, the wave momentum and the vortex momentum are then matched in the same ratio. Thus, for $n=1$ all momentum is in the waves, for $n=2$ there is equipartition, and for $n=3$ wave momentum is $1/2$ of the vortex momentum. The water strider case can be shown to follow the three-dimensional ratio and together with global momentum conservation this gives the main result as stated above.

The theoretical steps leading to these results are straightforward provided attention is paid to the usual difficulty of incompressible fluid momentum budgets in unbounded domains, namely that the momentum integrals are not absolutely convergent and thus that the momentum budget for infinite control region depends on the shape of the control region (e.g. Theodorsen 1941). This ambiguity can be clarified by considering the limiting case of weak compressibility.

The momentum budget of an impulsively forced wave pulse is simpler than the momentum budget of a slowly varying wavetrain. This is because the wave pulse contains a well-defined momentum at first order in wave amplitude whereas the first-order momentum of an oscillatory wavetrain is zero on average. The attempt to give the wavetrain a well-defined second-order 'wave momentum' leads to the so-called pseudomomentum of a wavetrain, and to the conceptual challenge of how to relate this pseudomomentum to the momentum and impulse budget of the entire flow (e.g. McIntyre 1981).

A second motivation for the present paper is precisely this conceptual challenge in the context of local wave–mean interaction theory, which is a theory that seeks to explain how localized wavepackets interact nonlinearly with the mean flow in which they are embedded (Bretherton 1969; Bühler & McIntyre 2003, 2005). A result that has emerged from these studies is a certain conservation law for the sum of wave pseudomomentum and vortex impulse, which is another example in which seemingly unrelated aspects of wave and vortex dynamics are coupled.

The plan of the paper is as follows. The classical linear theory for the impulsive forcing of unbounded incompressible fluids with spatial dimension $n = 1, 2, 3$ is presented in § 2 (with specific connections to Kelvin's impulse and experimental momentum measurement techniques discussed in § 2.5) and then adapted to weakly compressible flow in § 3 and to incompressible flows with a free surface in § 4. This involves a careful study of the wave emission process by which the flow adjusts to its steady vorticity-controlled end state. The water strider locomotion is then discussed in § 5 and concluding remarks are given in § 6.

The general remarks given in this introduction are sufficient to allow readers who are primarily interested in the water strider results to skip directly to § 5.

2. Incompressible flow

2.1. *Incompressible momentum budget*

We begin by noting some elementary facts about the momentum budget of an ideal incompressible homogeneous fluid subject to an external force per unit mass $\tilde{\boldsymbol{F}}$. For the most part we consider the fluid to be unbounded such that the n-dimensional position vector $\boldsymbol{x} \in R^n$. The governing equations are

$$\nabla \cdot \boldsymbol{u} = 0 \quad \text{and} \quad \frac{\mathrm{D}\boldsymbol{u}}{\mathrm{D}t} + \frac{\nabla \tilde{p}}{\rho} = \tilde{\boldsymbol{F}}, \tag{2.1}$$

where $\boldsymbol{u}$ is the velocity, $\tilde{p}$ is the pressure, and ρ is the homogeneous density, which is now set to unity without loss of generality.

We are interested in the integral momentum budget for a Eulerian control region $\mathscr{D} \subset R^n$ with boundary $\partial\mathscr{D}$, which is

$$\left.\begin{aligned} &\frac{\mathrm{d}}{\mathrm{d}t}\int_{\mathscr{D}} \boldsymbol{u}\,\mathrm{d}V + \oint_{\partial\mathscr{D}} (\boldsymbol{u}\boldsymbol{u}\cdot\boldsymbol{n} + \tilde{p}\boldsymbol{n})\,\mathrm{d}A = \int_{\mathscr{D}} \tilde{\boldsymbol{F}}\,\mathrm{d}V \\ \text{or} \qquad &\\ &\frac{\mathrm{d}}{\mathrm{d}t}\boldsymbol{M} + \tilde{\boldsymbol{\Phi}} = \tilde{\boldsymbol{R}}. \end{aligned}\right\} \tag{2.2}$$

Here $\boldsymbol{n}$ is the outward unit normal vector on $\partial\mathscr{D}$, $\boldsymbol{M}$ is the momentum contained in $\mathscr{D}$, $\tilde{\boldsymbol{\Phi}}$ is the momentum flux out of $\partial\mathscr{D}$, and $\tilde{\boldsymbol{R}}$ is the momentum per unit time that the external force adds to $\mathscr{D}$. This budget is unambiguous for finite-sized $\mathscr{D}$, but typically

the integrals are not absolutely convergent as $\mathscr{D}$ grows to infinity. Consequently, their limiting values as $\mathscr{D} \to \infty$ typically depend on the shape of $\mathscr{D}$ (§ 119 in Lamb 1932; Theodorsen 1941).

It is clear from (2.2) that for given $\mathscr{D}$ and given external forcing $\tilde{\boldsymbol{F}}$ the fluid response in $\mathscr{D}$ is partly momentum change as measured by $\mathrm{d}\boldsymbol{M}/\mathrm{d}t$ and partly momentum flux as measured by $\tilde{\boldsymbol{\Phi}}$. The sum of these two responses must equal $\tilde{\boldsymbol{R}}$ but it is not clear *a priori* how $\tilde{\boldsymbol{R}}$ is partitioned between the two. This is the basic question to be discussed here in the simple case of localized impulsive forcing.

2.2. *Localized impulsive forcing*

A well-known classical problem (e.g. Lamb 1932) describes the response of a resting fluid to an impulsive force at $t = 0$. That is, we consider external forces of the form

$$\tilde{\boldsymbol{F}}(\boldsymbol{x}, t) = \boldsymbol{F}(\boldsymbol{x}) \frac{1}{\Delta t} g(t/\Delta t) \tag{2.3}$$

in the limit of infinitesimal forcing duration $\Delta t \to 0$. Here the requirements on the function $g(s)$ are that it is non-negative, zero for $s < 0$ and $s > 1$, and has unit integral. Therefore, in the limit $\Delta t \to 0$ the forcing becomes a delta function in time and this is the definition of impulsive forcing. The classical argument then shows that during $t \in [0, \Delta t]$ the forcing magnitude and fluid acceleration are both large (i.e. $|\tilde{\boldsymbol{F}}| \sim |\boldsymbol{u}_t| = O(\Delta t^{-1})$), that the velocity is finite (i.e. $|\boldsymbol{u}| = O(1)$), and therefore that the quadratic term $(\boldsymbol{u} \cdot \nabla)\boldsymbol{u} = O(1)$ in the material derivative is negligible compared to the forcing and pressure terms. By the same argument the impulsive momentum flux $\tilde{\boldsymbol{\Phi}}$ is entirely due to pressure. Overall, this scaling argument shows that the impulsive forcing problem reduces to a linear set of equations, which can be solved with elementary methods.

The classical impulse theory holds for arbitrary spatial structure $\boldsymbol{F}(\boldsymbol{x})$ of the impulsive force. In the present context we restrict to localized forces, i.e. forces that have compact support and hence are non-zero only within a finite-sized region around the origin. Specifically, we require that there exists a length $L < \infty$ such that

$$r = |\boldsymbol{x}| > L \;\Rightarrow\; |\boldsymbol{F}(\boldsymbol{x})| = 0. \tag{2.4}$$

The restriction to localized forces is motivated physically and brings with it many mathematical simplifications, e.g. it ensures that all spatial moments of $\boldsymbol{F}$ are finite provided $|\boldsymbol{F}|$ is integrable, which we shall assume to be the case.

The impulsive momentum flux $\tilde{\boldsymbol{\Phi}}$ requires the pressure distribution $\tilde{p}$, which as usual is determined by taking the divergence of the momentum equation and using $(\nabla \cdot \boldsymbol{u})_t = 0$. Because the nonlinear terms are negligible this yields the simple Poisson equation

$$\nabla^2 \tilde{p} = \nabla \cdot \tilde{\boldsymbol{F}} = \nabla \cdot \boldsymbol{F} \, \frac{1}{\Delta t} g(t/\Delta t) \tag{2.5}$$

together with the boundary condition $\nabla \tilde{p} \to 0$ as $r \to \infty$. Therefore the impulsive pressure $\tilde{p}$ has the same delta-sequence time dependence as $\tilde{\boldsymbol{F}}$, i.e.

$$\tilde{p} = p(\boldsymbol{x}) \frac{1}{\Delta t} g(t/\Delta t) \quad \text{and} \quad \nabla^2 p = \nabla \cdot \boldsymbol{F}. \tag{2.6a, b}$$

By the assumptions on $g(s)$, p equals the time integral of $\tilde{p}$ over the forcing duration Δt. Indeed, the linear momentum equation can be time-integrated from $t = 0$ to $t = \Delta t$ to yield the simple expression

$$t = \Delta t\colon \quad \boldsymbol{u}(\boldsymbol{x}, \Delta t) + \nabla p(\boldsymbol{x}) = \boldsymbol{F}(\boldsymbol{x}) \tag{2.7}$$

for the velocity directly after the forcing. In the impulsive limit $\Delta t \to 0$ this expression furnishes the initial conditions at $t = 0+$ for the subsequent evolution of $\boldsymbol{u}$ without forcing. As can be easily shown by using Fourier transforms, (2.7) together with (2.6*b*) is equivalent to defining $\boldsymbol{u}(\boldsymbol{x}, \Delta t)$ as the least-square projection of $\boldsymbol{F}$ onto non-divergent vector fields.

Similarly, the time-integral of (2.2) over the forcing duration takes a simple form in terms of the quantities

$$\boldsymbol{\Phi} = \int_0^{\Delta t} \tilde{\boldsymbol{\Phi}}\, \mathrm{d}t \quad \text{and} \quad \boldsymbol{R} = \int_0^{\Delta t} \tilde{\boldsymbol{R}}\, \mathrm{d}t, \tag{2.8}$$

namely

$$t = \Delta t\colon \quad \boldsymbol{M}(\Delta t) + \boldsymbol{\Phi} = \boldsymbol{R}. \tag{2.9}$$

Thus $\boldsymbol{M}(\Delta t)$ is the fluid momentum contained in $\mathscr{D}$ after the impulsive forcing and $\boldsymbol{\Phi}$ is the time-integrated momentum flux across $\partial\mathscr{D}$ during the impulsive forcing. For convenience, we will often denote by $\boldsymbol{M}$ the value of $\boldsymbol{M}(\Delta t)$ as $\Delta t \to 0$. We shall be particularly interested in the limit of (2.9) as $\mathscr{D} \to \infty$ whilst preserving its shape.† In view of what has been said in the introduction, in the present case the wave field is associated with the pressure response to the forcing. Therefore, its contribution to the momentum budget is $\boldsymbol{\Phi}$ and the vortex contribution is $\boldsymbol{M}$.

The basic question noted before can now be posed succinctly: for a given force structure $\boldsymbol{F}(\boldsymbol{x})$, how is the total impulsive momentum input $\boldsymbol{R}$ partitioned into fluid momentum $\boldsymbol{M}$ and time-integrated momentum flux $\boldsymbol{\Phi}$?

As demonstrated below, the answer does not depend on the structure of $\boldsymbol{F}(\boldsymbol{x})$, but it does depends both on the number of spatial dimensions n and on the shape of $\mathscr{D}$ (Theodorsen 1941). Specifically, for a spherical control volume $\mathscr{D}$ the answer is

$$\boldsymbol{M} = \frac{n-1}{n}\boldsymbol{R} \quad \text{and} \quad \boldsymbol{\Phi} = \frac{1}{n}\boldsymbol{R}, \tag{2.10a, b}$$

i.e. in one dimension all momentum is carried away by the impulsive momentum flux, but only half of it is carried away in two dimensions, and only a third of it in three dimensions.‡ We shall now demonstrate these results using elementary computations and then move on to compressible flows.

2.3. *One-dimensional incompressible flow*

It is clear *a priori* that there are no vortices in one-dimensional fluid dynamics and therefore this section simply demonstrates that impulsive pressure fields can carry momentum away to infinity. In the one-dimensional problem with position x the incompressibility condition is $u_x = 0$ and therefore u depends on t only. In an unbounded domain any non-zero u therefore implies infinite momentum. It follows that for finite momentum input R there can be no acceleration whatsoever and thus $M = 0$ and $\Phi = R$ for any interval $\mathscr{D}$. Indeed, the pressure field with the correct

† This limit can be formally defined in terms of a family of domains $\mathscr{D}(\alpha)$ such that if the boundary $\partial\mathscr{D}(0)$ is the set of positions $\boldsymbol{x}$ satisfying $f(\boldsymbol{x}) = 0$ for a suitable level-set function f then the boundary $\partial\mathscr{D}(\alpha)$ corresponds to $f(\boldsymbol{x}/\alpha) = 0$. The limit $\mathscr{D} \to \infty$ then refers to $\mathscr{D}(\alpha)$ as $\alpha \to \infty$.

‡ The view that $\boldsymbol{u}$ is the projection of $\boldsymbol{F}$ onto non-divergent vector fields allows an interesting alternative derivation of (2.10) based on the usual projection formula for Fourier transforms $\widehat{\boldsymbol{u}} = (\boldsymbol{I} - \boldsymbol{k}\boldsymbol{k}/|\boldsymbol{k}|^2)\cdot\widehat{\boldsymbol{F}}$. Here the values of $(\widehat{\boldsymbol{u}}, \widehat{\boldsymbol{F}})$ at $\boldsymbol{k} = 0$ can be identified with $(\boldsymbol{M}, \boldsymbol{R})$ and for $n > 1$ the projector is clearly indeterminate as $\boldsymbol{k} \to 0$, as it has to be. By averaging over all possible orientations of $\boldsymbol{k}$ as $\boldsymbol{k} \to 0$ the expression (2.10*a*) is obtained.

boundary condition $p_x \to 0$ as $|x| \to \infty$ is

$$p(x) = p(-\infty) + \int_{-\infty}^{x} F(x')\,\mathrm{d}x' \tag{2.11}$$

and if F is localized at the origin then the pressure is

$$p = \frac{R}{2}\mathrm{sgn}(x) \quad \text{for} \quad |x| > L \tag{2.12}$$

after adjusting the irrelevant global pressure constant. Clearly, the one-dimensional case is very special because p does not decay with distance from the site of the forcing at the origin. Therefore, if $\mathscr{D}$ is any interval between x_L and x_R such that $x_L < -L$ and $x_R > L$ then

$$\Phi = p(x_R) - p(x_L) = \frac{R}{2} + \frac{R}{2} = R \tag{2.13}$$

as anticipated. This shows that in the one-dimensional case all momentum input is unambiguously fluxed away by the pressure wave.

2.4. *Two- and three-dimensional incompressible flow*

For $n > 1$ the pressure is computed from the Poisson equation

$$\nabla^2 p = \nabla \cdot \boldsymbol{F} \quad \text{subject to} \quad \nabla p \to 0 \quad \text{as} \quad r = |\boldsymbol{x}| \to \infty \tag{2.14}$$

by using the Green's function $G(\boldsymbol{x}, \boldsymbol{x}')$ that solves

$$\nabla^2 G = \delta(\boldsymbol{x} - \boldsymbol{x}') \quad \text{subject to} \quad \nabla G \to 0 \quad \text{as} \quad r = |\boldsymbol{x}| \to \infty. \tag{2.15}$$

This Green's function is

$$G(\boldsymbol{x}, \boldsymbol{x}') = \begin{cases} +\dfrac{1}{2\pi}\ln|\boldsymbol{x} - \boldsymbol{x}'| & (n = 2) \\ -\dfrac{1}{4\pi}|\boldsymbol{x} - \boldsymbol{x}'|^{-1} & (n = 3) \end{cases} \tag{2.16}$$

and the pressure p is then given by the convolution

$$p(\boldsymbol{x}) = \int G(\boldsymbol{x}, \boldsymbol{x}')\nabla' \cdot \boldsymbol{F}'\,\mathrm{d}V' = -\int \boldsymbol{F}' \cdot \nabla' G(\boldsymbol{x}, \boldsymbol{x}')\,\mathrm{d}V'. \tag{2.17a, b}$$

Here the integral extends formally over all $\boldsymbol{x}' \in R^n$ and the primes indicate that the functions and differential operators relate to $\boldsymbol{x}'$. The special second form follows from the divergence theorem together with the compactness of $\boldsymbol{F}'(\boldsymbol{x}')$.

Only the far-field asymptotics of $p(\boldsymbol{x})$ are needed to compute the momentum flux

$$\boldsymbol{\Phi} = \oint_{\partial\mathscr{D}} p\boldsymbol{n}\,\mathrm{d}A \tag{2.18}$$

in the targeted limit $\mathscr{D} \to \infty$. Specifically, only the dipolar part of p (which decays as r^{1-n}) is relevant for $\boldsymbol{\Phi}$ in the far field $r \gg L$. The dipolar part of p can be extracted from (2.17) by using the standard multipole expansion for the far-field region $r \gg L$. In this region the Green's function is slowly varying in $\boldsymbol{x}'$ and G can be Taylor-expanded as

$$G(\boldsymbol{x}, \boldsymbol{x}') = G(\boldsymbol{x}, 0) + \boldsymbol{x}' \cdot \nabla' G(\boldsymbol{x}, 0) + \cdots, \tag{2.19}$$

which upon substitution in (2.17) yields the coefficients of the far-field multipole expansion. The first term does not depend on $\boldsymbol{x}'$ and therefore makes no contribution

in (2.17*b*) and the second term gives the dipolar term (cf. (1.1))

$$p \approx -\int \boldsymbol{F}' \,\mathrm{d}V' \cdot \nabla' G(\boldsymbol{x}, 0) = -\boldsymbol{R} \cdot \nabla' G(\boldsymbol{x}, 0) \quad \text{as} \quad r \to \infty. \tag{2.20}$$

Now, the symmetries of the Poisson equation in an unbounded domain imply that $G(\boldsymbol{x}, \boldsymbol{x}') = G(|\boldsymbol{x} - \boldsymbol{x}'|)$ and therefore $-\nabla' G(\boldsymbol{x}, \boldsymbol{x}') = +\nabla G(\boldsymbol{x}, \boldsymbol{x}')$. With the shorthand

$$G_0(\boldsymbol{x}) \equiv G(\boldsymbol{x}, 0) = \begin{cases} +\dfrac{1}{2\pi} \ln r & (n = 2) \\ -\dfrac{1}{4\pi} r^{-1} & (n = 3) \end{cases} \tag{2.21}$$

the leading-order far-field pressure therefore takes the final form $p \approx \boldsymbol{R} \cdot \nabla G_0(\boldsymbol{x})$, which is

$$p \approx \frac{1}{2\pi r} \frac{\boldsymbol{R} \cdot \boldsymbol{x}}{r} \quad \text{for} \quad n = 2 \quad \text{and} \quad p \approx \frac{1}{4\pi r^2} \frac{\boldsymbol{R} \cdot \boldsymbol{x}}{r} \quad \text{for} \quad n = 3, \tag{2.22}$$

both with error $O(r^{-n})$ as $r \to \infty$. Higher-order terms in the multipole expansion affect the momentum flux at finite r but become irrelevant as $r \to \infty$.

Thus only $\boldsymbol{R}$, i.e. the zeroth spatial moment of $\boldsymbol{F}$, affects the dipolar part of p in the far field. In other words, the structure of $\boldsymbol{F}(\boldsymbol{x})$ is irrelevant, only its total integral matters. The limiting momentum flux $\boldsymbol{\Phi}$ is easily computed for a spherically symmetric control volume $\mathscr{D}$. For instance, in the case $n = 2$ we can align $\boldsymbol{R}$ with the x-axis and then use cylindrical coordinates such that $(x, y) = (r\cos\theta, r\sin\theta)$ to evaluate (2.18) for a large circle with radius $r \gg L$ as

$$\boldsymbol{\Phi} = \int_0^{2\pi} \frac{R\cos\theta}{2\pi r} (\cos\theta, \sin\theta)\, r \,\mathrm{d}\theta = \frac{R}{2}(1, 0) = \frac{\boldsymbol{R}}{2} \tag{2.23}$$

with error $O(r^{-1})$. A precisely analogous computation in the case $n = 3$ using spherical coordinates yields $\boldsymbol{\Phi} = \boldsymbol{R}/3$ in accordance with (2.10).

The previously mentioned dependence of $\boldsymbol{\Phi}$ on the shape of $\mathscr{D}$ is easily demonstrated in the case $n = 2$ by using a rectangular control volume $|x| \leqslant a$ and $|y| \leqslant b$ (Theodorsen 1941). The limit $\mathscr{D} \to \infty$ then corresponds to $b \to \infty$ with a/b fixed. With $\boldsymbol{R}$ aligned with the x-axis as before, the limiting y-component of the momentum flux is zero whilst its x-component is

$$2\int_{-b}^{+b} p(a, y)\,\mathrm{d}y = \frac{2R}{2\pi} \int_{-b}^{+b} \frac{a}{a^2 + y^2}\,\mathrm{d}y = \frac{2R}{\pi} \arctan(b/a). \tag{2.24}$$

The previous result $\boldsymbol{\Phi} = \boldsymbol{R}/2$ for a circular control volume agrees with this formula only if $a = b$, which corresponds to a square. If $a \neq b$ then the crucial 90° symmetry is lost and (2.24) differs from (2.23).

In particular, if $b \ll a$ then $\boldsymbol{\Phi} \approx 0$ whereas if $b \gg a$ then $\boldsymbol{\Phi} \approx \boldsymbol{R}$. In the light of the identity (2.9) this shows that for a wide and thin rectangle $\mathscr{D}$ aligned with $\boldsymbol{R}$ all the external momentum input $\boldsymbol{R}$ appears as fluid momentum $\boldsymbol{M}$ and the pressure-induced momentum flux $\boldsymbol{\Phi}$ to infinity is zero. On the other hand, if the same control rectangle is rotated by 90° then precisely the opposite partition would be observed. This is illustrated in figure 1.

With the pressure now determined the velocity field $\boldsymbol{u}$ at $t = 0+$ can be computed directly from (2.7). Alternatively, $\boldsymbol{u}$ can be computed from $\nabla \times \boldsymbol{u} = \nabla \times \boldsymbol{F}$ and $\nabla \cdot \boldsymbol{u} = 0$. In two dimensions this is particularly simple; it means finding the streamfunction ψ

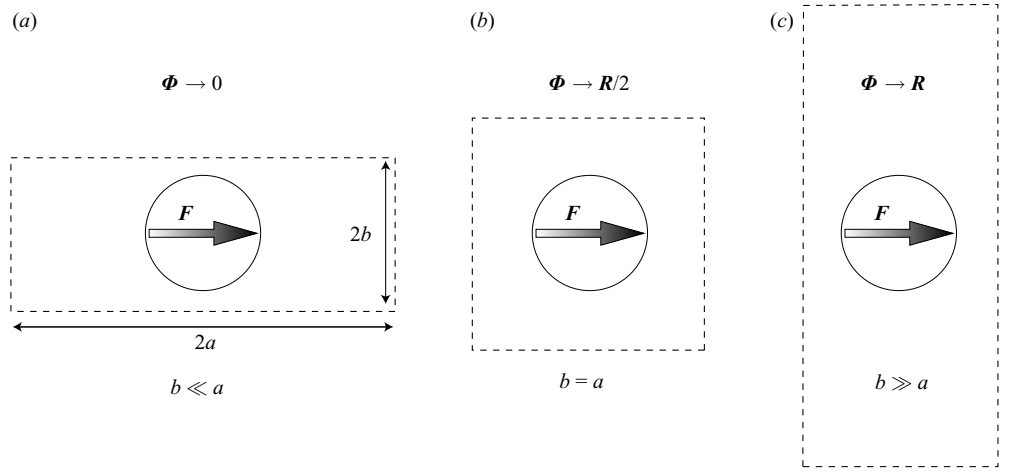

FIGURE 1. Two-dimensional schematic illustrating the dependence of $\boldsymbol{\Phi}$ on the shape of $\mathscr{D}$ as $\mathscr{D} \to \infty$. The force field $\boldsymbol{F}$ is indicated by the arrow and the circle has radius L and indicates the support of $\boldsymbol{F}$. The dashed lines indicate different shapes of $\mathscr{D}$. (*a*) A wide and thin rectangle leads to $\boldsymbol{\Phi} \to 0$. (*b*) A square leads to $\boldsymbol{\Phi} \to \boldsymbol{R}/2$. (*c*) A tall and narrow rectangle leads to $\boldsymbol{\Phi} \to \boldsymbol{R}$. In all cases $\boldsymbol{M} = \boldsymbol{R} - \boldsymbol{\Phi}$.

such that

$$\boldsymbol{u} = \widehat{\boldsymbol{z}} \times \nabla\psi \quad \text{and} \quad \nabla^2\psi = \widehat{\boldsymbol{z}} \cdot \nabla \times \boldsymbol{F} \quad \text{subject to} \quad \nabla\psi \to 0 \quad \text{as} \quad r \to \infty. \tag{2.25}$$

This is identical to the pressure equation (2.14) after rotating the $\boldsymbol{F}$ in (2.14) clockwise by 90°. Therefore the streamfunction ψ is equal to the pressure field p rotated clockwise by 90°, i.e.

$$\psi(x, y) = p(-y, x) \tag{2.26}$$

with a corresponding dipolar far-field expansion for ψ. The momentum content $\boldsymbol{M}$ in $\mathscr{D}$ can be written as an integral of ψ over $\partial\mathscr{D}$, and the 90° symmetry between ψ and p thus makes clear why in the two-dimensional case $\boldsymbol{M} = \boldsymbol{\Phi}$ for all $\mathscr{D}$ that also have this symmetry. An analogous statement holds in the three-dimensional case.

These examples of impulsive forcing of an incompressible fluid make clear the basic working of the theory. In a nutshell, impulsive localized fluid forcing always creates a global fluid response with corresponding global momentum fluxes, and these momentum fluxes decay with distance r from the forcing site such that the only relevant component of the momentum flux as $r \to \infty$ is its dipolar part. In turn, the magnitude of this dipolar part depends only on the integrated momentum input $\boldsymbol{R}$ of the localized force $\boldsymbol{F}$. Therefore, the far-field momentum flux can be computed as if the impulsive force were perfectly localized, i.e. as if $\tilde{\boldsymbol{F}} = \boldsymbol{R}\delta(t)\delta(\boldsymbol{x})$, and it is this simple generic form that makes possible the generality of the momentum decomposition results.

2.5. *Kelvin's impulse, trapped fluid momentum, and their use in experiments*

The ambiguity of the incompressible momentum budget makes it difficult to extract, say, an estimate for $\boldsymbol{R}$ from observations of impulsive fluid motion in an experiment. Fortunately, these difficulties can be side-stepped by using the theory of Kelvin's hydrodynamic impulse, which establishes an unambiguous link between $\boldsymbol{R}$ and the impulsively forced vorticity field. The vorticity is localized if $\boldsymbol{F}$ is, and it can be measured using particle velocimetry techniques and is thus accessible to experiment.

However, this is a complex and expensive technique. A simpler and cheaper technique is flow visualization, which allows direct observation not of the vorticity but of the movement of fluid trapped inside the vortices. It turns out that the momentum of this trapped fluid can be linked to $\boldsymbol{R}$ as well and this again allows estimation of $\boldsymbol{R}$ from flow data. Because of their importance to experiments these concepts are briefly discussed in the present section.

By definition, for $n > 1$ Kelvin's hydrodynamic impulse is the rotated first moment of a localized vorticity field:

$$\boldsymbol{I}(t) \equiv \frac{1}{n-1} \int_{\mathscr{D}} \boldsymbol{x} \times (\nabla \times \boldsymbol{u}) \, \mathrm{d}V. \tag{2.27}$$

Here the requirement on $\mathscr{D}$ is that it be large enough to include the support of $\nabla \times \boldsymbol{u}$. Using integration by parts and decay conditions at infinity the rate of change of $\boldsymbol{I}$ subject to a localized force $\tilde{\boldsymbol{F}}$ is computed as (e.g. Batchelor 1967)

$$\frac{\mathrm{d}\boldsymbol{I}}{\mathrm{d}t} = \frac{1}{n-1} \int_{\mathscr{D}} \boldsymbol{x} \times (\nabla \times \tilde{\boldsymbol{F}}) \, \mathrm{d}V = \int_{\mathscr{D}} \tilde{\boldsymbol{F}} \, \mathrm{d}V = \tilde{\boldsymbol{R}}. \tag{2.28}$$

This result holds without ambiguity for $n > 1$ and for all shapes of $\mathscr{D}$. It is also not restricted to the linearized equations. In the special case of impulsive forcing from rest (2.28) implies that $\boldsymbol{I}(t) = \boldsymbol{R}$ for all $t > 0$. There is no unique relationship between impulse $\boldsymbol{I}$ and momentum $\boldsymbol{M}$ as $\mathscr{D} \to \infty$, because $\boldsymbol{M}$ depends on the shape of $\mathscr{D}$ whereas $\boldsymbol{I}$ does not. For spherical control volumes $(n-1)\boldsymbol{I} = n\boldsymbol{M}$.

The Kelvin impulse theory shows that the momentum input by an external force can be determined from knowledge of the vorticity field alone, i.e. without having to compute the pressure field at all. This is useful for experiments in which vortices might be easier to measure than waves. Using the vorticity distribution to deduce the recoil force $\boldsymbol{R}$ is particularly easy if the vorticity takes a simple form such as a two-dimensional propagating dipole or a three-dimensional spherical vortex or vortex ring. For these forms analytical expressions are known that relate $\boldsymbol{I}$ to a few parameters such as vortex size and circulation strength (e.g. Batchelor 1967, § 7.2–7.3). For instance, this approach has been used in Drucker & Lauder (1999) to estimate the force balance on a swimming fish by observing the vortex rings in its wake using digital particle image velocimetry.

As noted before, another experimental technique to approximate $\boldsymbol{R}$ in the case of simple dipolar vorticity structures is to measure the momentum, $\boldsymbol{M}_v$ say, of the trapped fluid that is travelling with the non-linear flow induced by the vortex structure (e.g. Hu *et al.* 2003). For instance, a two-dimensional vortex dipole travels nonlinearly with a speed proportional to its dipole moment and it carries a mass of fluid with it that is trapped inside a closed streamline if the flow is viewed in a frame moving with the vortex. The same is true for three-dimensional vortex dipoles such as Hill's spherical vortex.

It is easy to check by comparing with known formulae (e.g. Batchelor 1967) that for spherical vortex dipoles the trapped fluid momentum $\boldsymbol{M}_v$ defined in this way is equal to the fluid momentum $\boldsymbol{M}$ computed for a large spherical control volume $\mathscr{D}$. This also shows that for non-spherical vortex dipoles $\boldsymbol{M}_v \neq \boldsymbol{M}$ in general. (For instance, in the case of a two-dimensional vortex dipole formed by two oppositely signed point vortices the trapped fluid region has a near-elliptical shape and one finds that $\boldsymbol{M}_v = 0.75\boldsymbol{M}$.) Therefore we obtain

$$\boldsymbol{M}_v = \frac{n-1}{n} \boldsymbol{R}, \tag{2.29}$$

but only for spherical vortices. This formula can be used to compute $\boldsymbol{R}$ from measurements of $\boldsymbol{M}_v$. The same formula also applies for horizontal fluid forcing in the presence of a free surface, which makes it relevant to the propulsion of water striders: the trapped fluid momentum in the hemispherical vortex is 2/3 of the recoil felt by the insect.

3. Compressible flow

It was shown in § 2 that the incompressible momentum budget depends on the shape of $\mathscr{D}$ as $\mathscr{D} \to \infty$. However, the incompressible theory offered no criterion for whether a specific shape of $\mathscr{D}$ might be physically more relevant than others. By introducing compressibility such a criterion is established because pressure waves caused by localized forcing naturally expand as spheres centred around the forcing site. This selects spherical control volumes $\mathscr{D}$ as the most physically relevant in the limit of weak compressibility. (Despite this physical argument for preferring spherical control volumes it should be noted that the incompressible results for, say, rectangular $\mathscr{D}$ are perfectly physical and could in principle be observed using rectangular arrays of pressure sensors.)

Physically, the introduction of compressibility removes the infinitely fast action-at-a-distance nature of the pressure field in a strictly incompressible fluid. Instead, the speed of the pressure wave is now bounded by the sound speed. This allows a better understanding of the physical adjustment process by which the fluid at a given position $\boldsymbol{x}$ is accelerated from rest to its final velocity. For localized impulsive forcing it turns out that the final adjusted velocity is equal to that given instantaneously by the incompressible theory. However, the velocity field can be quite different during the adjustment period. The differences are especially pronounced in the two-dimensional case. The presence of a time-dependent adjustment process also plays an important role in the free-surface problem considered in § 4 below.

3.1. *Compressible equations*

Compressibility is introduced in the simplest way, i.e. by replacing $\nabla \cdot \boldsymbol{u} = 0$ with the full continuity equation

$$\frac{\mathrm{D}\rho}{\mathrm{D}t} + \rho \nabla \cdot \boldsymbol{u} = 0 \tag{3.1}$$

and by making the pressure a function of ρ, i.e. $p = f(\rho)$. Only the linear problem is tractable analytically and therefore the equations are linearized around a uniform state of rest and unit density, i.e.

$$\boldsymbol{u} = \epsilon \boldsymbol{u}', \quad \rho = 1 + \epsilon \rho', \quad \tilde{p} = f(1) + \epsilon \tilde{p}', \quad \tilde{\boldsymbol{F}} = \epsilon \tilde{\boldsymbol{F}}' \tag{3.2}$$

with $\epsilon \ll 1$. Substitution in the governing equations gives the linear system at $O(\epsilon)$:

$$\boldsymbol{u}'_t + c^2 \nabla \rho' = \tilde{\boldsymbol{F}}', \tag{3.3}$$

$$\rho'_t + \nabla \cdot \boldsymbol{u}' = 0. \tag{3.4}$$

Here the sound speed squared $c^2 = f'(1)$ such that $\tilde{p}' = c^2 \rho'$. The linear equations can be decomposed explicitly into a vortex and a wave part via

$$\nabla \times \boldsymbol{u}'_t = \nabla \times \tilde{\boldsymbol{F}}', \tag{3.5}$$

$$\rho'_{tt} - c^2 \nabla^2 \rho' = -\nabla \cdot \tilde{\boldsymbol{F}}'. \tag{3.6}$$

We seek to compute the linear response of a fluid at rest to the impulsive force

$$\tilde{\boldsymbol{F}}' = \boldsymbol{F}'(\boldsymbol{x})\delta(t). \tag{3.7}$$

Now, the impulsive response of a compressible fluid differs greatly from that of an incompressible fluid. In fact, it is much simpler. This is because the impulsive force acts too quickly to change the density or pressure field, which are proportional to particle displacements. For finite forcing duration Δt these displacements are $O(\Delta t)$ and hence they become negligible in the limit $\Delta t \to 0$. On the other hand, the velocity field in (3.3) can change impulsively and it becomes simply $\boldsymbol{u}' = \boldsymbol{F}'$ at $t = 0+$.

Thus, the impulsively forced problem with zero initial conditions is equivalent to an unforced initial-value problem with non-zero initial conditions on the velocity:

$$\boldsymbol{u}'(\boldsymbol{x}, 0+) = \boldsymbol{u}'_0 = \boldsymbol{F}' \quad \text{and} \quad \rho'(\boldsymbol{x}, 0+) = \rho'_0 = 0. \tag{3.8}$$

Notice that the wave equation (3.6) for ρ' is decoupled from $\boldsymbol{u}'$ and can be solved on its own subject to the implied initial conditions

$$\rho'_0 = 0 \quad \text{and} \quad (\rho'_t)_0 = -\nabla \cdot \boldsymbol{u}'_0 = -\nabla \cdot \boldsymbol{F}'. \tag{3.9}$$

The quantity of most interest from the linear solution is the compressible integral momentum budget for a control volume $\mathscr{D}$:

$$\frac{\mathrm{d}}{\mathrm{d}t} \int_{\mathscr{D}} \boldsymbol{u}' \,\mathrm{d}V + \oint_{\partial \mathscr{D}} c^2 \rho' \boldsymbol{n} \,\mathrm{d}A = \int_{\mathscr{D}} \tilde{\boldsymbol{F}}' \,\mathrm{d}V. \tag{3.10}$$

We will consider the solution to this problem for a delta-function force

$$\boldsymbol{F}' = \boldsymbol{R}\delta(\boldsymbol{x}). \tag{3.11}$$

It is clear *a priori* that at a time $t > 0$ all momentum is necessarily contained in a sphere with radius ct around the origin. This is because the wave front travels with speed c and there can be no disturbance ahead of the wave front. In other words, for any finite time t the introduction of compressibility has removed the ambiguity of the incompressible momentum budget.

3.2. *One-dimensional and three-dimensional compressible flow*

As usual, the solution of the wave equation is simple if $n = 1$ or $n = 3$ and more complex if $n = 2$. Dropping primes on linear variables, the one-dimensional problem with $u_0 = R\delta(x)$ and $\rho_0 = 0$ has the solution

$$u(x, t) = \frac{R}{2}\{\delta(ct - x) + \delta(ct + x)\}, \tag{3.12}$$

$$\tilde{p}(x, t) = c^2 \rho(x, t) = \frac{cR}{2}\{\delta(ct - x) - \delta(ct + x)\}. \tag{3.13}$$

All momentum is bound to the two sharp fronts at $|x| = ct$ and the velocity has the same sign as R at both fronts. The pressure field is also confined to the fronts but differs in sign such that for $R > 0$ a positive pressure pulse is travelling to the right and vice versa. The time-integral of $\tilde{p}$ at fixed $x \neq 0$ is

$$p = \int_0^t \tilde{p} \,\mathrm{d}\tau = \frac{R}{2}\mathrm{sgn}(x) H(ct - |x|), \tag{3.14}$$

which for $ct > |x|$ agrees with the time-integrated incompressible pressure pulse in (2.12). Away from the origin $u = -p_x$ and the gradient of (3.14) then confirms that all momentum is bound to the wave front.

By definition, the momentum of a body of fluid equals its mass times the velocity of its centre of mass and therefore the fluid should be continually moving in the direction of R. This did not happen in the incompressible case because the relevant fluid mass was infinite there. In the compressible case the fluid mass containing non-zero momentum is bounded at all times and therefore there should be a discernible non-zero fluid displacement. Indeed, defining the linear particle displacement $\xi(x,t)$ by

$$\xi_t = u \quad \text{and} \quad \xi(x,0) = 0 \quad \text{yields} \quad \xi = \frac{R}{2c} H(ct - |x|). \tag{3.15}$$

This rather pleasing result shows that fluid particles suffer a net displacement of $R/2c$ as the wave front arrives. At time t the interval of displaced particles has length $2ct$ and therefore the x-integrated fluid displacement equals Rt and its rate of change equals the net momentum R, as it should. The singular character of the limit $c \to \infty$ is apparent here: the individual particle displacement ξ goes to zero but the collective x-integrated displacement remains finite.

In three dimensions the fundamental solution to the wave equation subject to initial data $\rho_0 = 0$ and $(\rho_t)_0 = \delta(\boldsymbol{x})$ is $\rho = \delta(ct - r)/(4\pi c^2 t)$. The solution for the specific initial data (3.9) is then obtained by differentiation as

$$\tilde{p}(\boldsymbol{x},t) = c^2 \rho(\boldsymbol{x},t) = -\frac{\boldsymbol{R}\cdot\nabla\delta(ct-r)}{4\pi t} = \frac{\boldsymbol{R}\cdot\boldsymbol{x}}{4\pi r t}\delta'(ct-r). \tag{3.16}$$

As before, all fluid acceleration for $t > 0$ is again confined to the sharp wave front $r = ct$. Indeed, as the front passes the fluid is impulsively accelerated from rest to the non-divergent velocity described by incompressible theory. The wave front acts like a curtain that unveils this balanced flow whilst travelling with speed c outwards.

The time-integrated pressure at fixed $r > 0$ is of dipolar form

$$p = \int_0^t \tilde{p}\,\mathrm{d}\tau = \int_0^t \frac{\boldsymbol{R}\cdot\boldsymbol{x}}{4\pi r\, c\tau}\delta'(c\tau - r)\, c\,\mathrm{d}\tau = \frac{\boldsymbol{R}\cdot\boldsymbol{x}}{4\pi r^3} H(ct-r) \tag{3.17}$$

and for $ct > r$ it agrees with (2.22). The velocity field away from the singularity at the origin is given by $\boldsymbol{u} = -\nabla p$ and it follows from (3.17) that the momentum contained in a shell $r_1 \leqslant r \leqslant r_2$ is exactly zero for all radii such that $0 < r_1 < r_2 < ct$. This means that for spherical control volumes all momentum is concentrated either at the singular origin $r = 0$ or at the wave front $r = ct$. Indeed, evaluating the momentum in a shell with $r_1 < ct$ and $r_2 > ct$ shows that the spherical wave front possesses a delta-function contribution of bound momentum with magnitude $\boldsymbol{R}/3$. This equals the amount of momentum that was fluxed across a spherical surface $\partial\mathscr{D} \to \infty$ in the incompressible case, as it must. The singular momentum at the origin therefore has magnitude $\boldsymbol{R}$ at time $t = 0$ and $2\boldsymbol{R}/3$ at all later times $t > 0$.

3.3. *Two-dimensional compressible flow*

The two-dimensional case is the *bête noire* of the wave equation family. Most importantly, in two dimensions the wave front is not sharp and the flow continues to adjust after the front has passed. Moreover, the flow adjustment is not monotone and typically includes a sign reversal of the velocity field.

In two dimensions the fundamental solution to the wave equation subject to initial data $\rho_0 = 0$ and $(\rho_t)_0 = \delta(\boldsymbol{x})$ is $\rho = H(ct - r)/(2\pi c\sqrt{c^2t^2 - r^2})$. The solution for the initial data (3.9) is

$$\tilde{p}(\boldsymbol{x},t) = c^2\rho(\boldsymbol{x},t) = -\frac{c\boldsymbol{R}\cdot\nabla}{2\pi}\frac{H(ct-r)}{\sqrt{c^2t^2-r^2}} = -\frac{c\boldsymbol{R}\cdot\boldsymbol{x}}{2\pi r}\frac{\partial}{\partial r}\left\{\frac{H(ct-r)}{\sqrt{c^2t^2-r^2}}\right\}. \tag{3.18}$$

The two-dimensional wave front is sharp towards the quiescent region $r > ct$ but the pressure and density are non-zero throughout the disturbed region, where

$$r < ct: \quad \tilde{p}(\boldsymbol{x}, t) = -\frac{c\boldsymbol{R}\cdot\boldsymbol{x}}{2\pi}\frac{1}{(c^2t^2 - r^2)^{3/2}} \tag{3.19}$$

holds. This non-uniform pressure field gradually decays as $t \to \infty$ and the same is true for the fluid acceleration in the disturbed region $r < ct$. This confirms that the two-dimensional velocity field asymptotes to its final state gradually rather than jumping to it instantaneously. Notably, the decaying pressure field for $r < ct$ has a dipolar structure that is opposite to that of the incompressible pressure pulse. For example, if $\boldsymbol{R}\cdot\boldsymbol{x} = Rx$ with $R > 0$ then $p > 0$ for $x < 0$ and vice versa, which corresponds to a gradually decaying positive x-acceleration on $y = 0$ (see figure 2 below).

The time-integrated pressure field p is more complex than before:

$$\begin{aligned} p &= -\frac{\boldsymbol{R}\cdot\boldsymbol{x}}{2\pi r}\frac{\partial}{\partial r}\left\{\int_0^t \frac{H(c\tau - r)c\mathrm{d}\tau}{\sqrt{c^2\tau^2 - r^2}}\right\} = -\frac{\boldsymbol{R}\cdot\boldsymbol{x}}{2\pi r}\frac{\partial}{\partial r}\left\{H(ct-r)\int_{r/c}^t \frac{c\mathrm{d}\tau}{\sqrt{c^2\tau^2 - r^2}}\right\} \\ &= -\frac{\boldsymbol{R}\cdot\boldsymbol{x}}{2\pi r}\frac{\partial}{\partial r}\left\{H(ct-r)\ln\frac{ct + \sqrt{c^2t^2 - r^2}}{r}\right\} \\ &= -\frac{\boldsymbol{R}\cdot\boldsymbol{x}}{2\pi r}H(ct-r)\frac{\partial}{\partial r}\left\{\ln\frac{ct + \sqrt{c^2t^2 - r^2}}{r}\right\}. \end{aligned}$$

In the last step the r-derivative of $H(ct - r)$ can be neglected because it produces a delta function at $r = ct$ that is multiplied by the vanishing logarithm at this location. The final result is

$$p = \frac{\boldsymbol{R}\cdot\boldsymbol{x}}{2\pi r^2}H(ct-r)\frac{ct}{\sqrt{c^2t^2 - r^2}}. \tag{3.20}$$

For fixed r and $t \to \infty$ this converges to the incompressible result (2.22), as it must.

The time-dependent momentum budget is illustrated by considering the time evolution of momentum $\boldsymbol{M}(t)$ that is contained in a circle of fixed radius r. Initially, $\boldsymbol{M}(0) = \boldsymbol{R}$ in response to the impulsive forcing. The change of $\boldsymbol{M}(t)$ from its initial value is equal to minus the flux integral of p along the circumference of the circle. Therefore

$$\boldsymbol{M}(t) = \boldsymbol{R}\left\{1 - \frac{1}{2}H(ct-r)\frac{ct}{\sqrt{c^2t^2 - r^2}}\right\}. \tag{3.21}$$

When the wave front crosses the circle at time $ct = r$ an infinite amount of bound momentum in the direction of $\boldsymbol{R}$ is exported and $\boldsymbol{M}(t)$ takes arbitrarily large values in the direction opposite to $\boldsymbol{R}$. These large negative values are then swiftly eroded, and $\boldsymbol{M}$ crosses zero at the time $ct = \sqrt{4/3}r$, and subsequently asymptotes towards $\boldsymbol{R}/2$. The time of zero crossing implies that for fixed time t the momentum contained in the region $\sqrt{3/4}\,ct \leqslant r$ is precisely equal to $\boldsymbol{R}$. This gives a rough guide to the width of the smeared-out wave front as $\Delta r \approx 0.15ct$.

The two-dimensional solution is illustrated in figure 2 using a numerical solution to the linear initial-value problem of the non-dispersive shallow water system, in which surface elevation is equivalent to density (see figure caption).

The oscillatory behaviour of $\boldsymbol{M}(t)$ is also observed in the time evolution of the velocity $\boldsymbol{u}$ at a fixed position x. For instance, if the $\boldsymbol{x}$-coordinate is aligned with $\boldsymbol{R}$ then the velocity at $x > 0$ on the centreline $y = 0$ first jumps to positive infinity as the wave front arrives, and then immediately jumps down to negative infinity. Thereafter

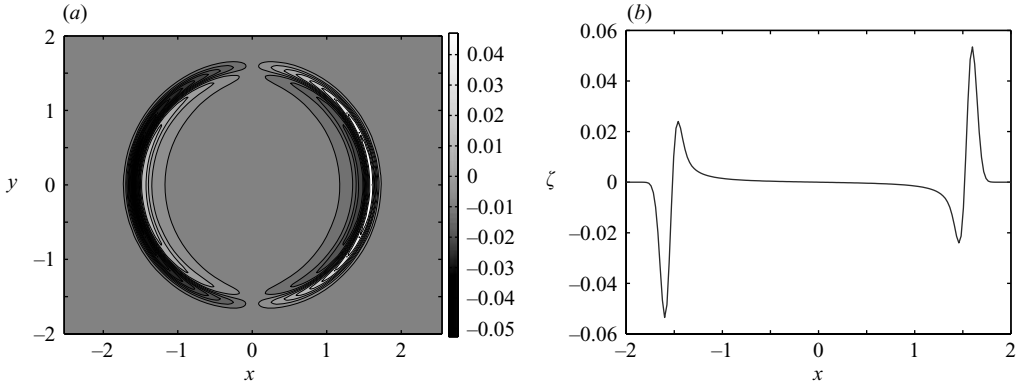

FIGURE 2. Numerical solution for impulsive response of linear shallow-water system with wave speed $c=\sqrt{gH}$ for gravity g and layer depth $H=1$ cm. The surface elevation ζ is equivalent to the density or pressure disturbance of a compressible fluid. Initial conditions are $\zeta(\boldsymbol{x},0)=0$ and $\zeta_t(\boldsymbol{x},0)=-\boldsymbol{\nabla}\cdot\boldsymbol{F}$ with Gaussian force $\boldsymbol{F}=(F,0)$ and $F=R/2\pi\sigma^2\exp(-(x^2+y^2)/2\sigma^2)$. The parameters are $R=0.5$ and $\sigma=0.05$ cm. (*a*) Surface elevation ζ at time $t=0.05$ in cgs units, showing dipolar structure and smeared-out wave front. (*b*) Elevation on $y=0$ at the same time. The wave front pressure is positive on the right and negative on the left and it is followed by an oppositely signed peak just behind the wave front. Both peaks tend to infinity as the forcing width $\sigma\to 0$. Also visible is the weaker negative pressure gradient in the interior.

it gradually asymptotes towards its final positive value (cf. figure 2). Of course, these localized infinities are caused by the delta-function form of the initial conditions and they disappear after convolution with smooth initial data, as shown in the figure. Nevertheless, they are indicative of the non-uniform and oscillatory manner in which the momentum is distributed in the two-dimensional case.

4. Free surface flow

We return to three-dimensional incompressible flow and add a free surface whose undisturbed rest location in Cartesian coordinates (x,y,z) is at $z=0$, say, where z is increasing upwards and gravity points downwards into the semi-infinite fluid. The free surface affects the response to impulsive forcing in two ways. First, the dynamical boundary condition at the free surface now demands that the fluid pressure at the surface matches the sum of the (constant) air pressure plus the mean surface curvature multiplied by the surface tension. Second, the presence of the free surface allows surface waves to exist and such waves can be excited by impulsive forcing. These dispersive surface waves are analogous to the non-dispersive sound waves in the compressible flows described in § 3. Their inevitable presence implies that we must distinguish clearly between the fluid state at $t=0+$, i.e. immediately after the impulsive forcing, and the fluid state at sufficiently long times such that the surface waves have propagated away from the region of interest. Indeed, just as in the compressible case, the impulsively generated state at $t=0+$ adjusts to a final steady state at $t=+\infty$ via the emission and outward propagation of surface waves.

Contrary to what one might expect, it turns out that gravity and surface tension can only affect the wave-related adjustment process. More precisely, non-zero values of gravity and/or surface tension are necessary in order to single out $z=0$ as the minimum-energy rest position of the free surface, but otherwise these values do not appear in either the computation of the fluid state at $t=0+$ or at $t=+\infty$. In essence,

it will be seen that this is because the impulsive forcing is by definition too rapid to involve any free-surface dynamics and because the final steady state is controlled solely by the vorticity of the fluid. These remarks are strictly true for impulsive forcing relative to a flat undisturbed free surface at $z=0$. Within linear theory, they are also true if the initial free surface is disturbed in an arbitrary way, because this disturbance could be accounted for by superimposing a suitable surface wave initial condition.

On the other hand, it will be seen that the fluid response at both $t=0+$ and $t=+\infty$ is profoundly affected by the air pressure part of the dynamical boundary condition at the free surface, which for a flat surface can be written as $\tilde{p}=0$. This will be important in the application of impulsive-forcing theory to water strider locomotion that follows in § 5.

4.1. *Impulsive pressure response with free surface*

We consider an impulsive force field localized at $x=y=0$ and depth $z=-h$ where $h>0$. Specifically,

$$\tilde{\boldsymbol{F}}(\boldsymbol{x},t)=\boldsymbol{F}(\boldsymbol{x})\delta(t)=\boldsymbol{R}\delta(x)\delta(y)\delta(z+h)\delta(t). \tag{4.1}$$

It will turn out that the exact value of $h>0$ does not affect the overall partitioning of momentum between waves and vortices, but it does affect the detailed structure of the flow. The impulsive pressure field $\tilde{p}=p(\boldsymbol{x})\delta(t)$ satisfies

$$\nabla^2 p=\nabla\cdot\boldsymbol{F}=\boldsymbol{R}\cdot\nabla\,\delta(x)\delta(y)\delta(z+h)\quad\text{subject to}\quad\begin{cases}p=0 & \text{at}\quad z=0\\ \nabla p\to 0 & \text{as}\quad r\to\infty.\end{cases} \tag{4.2}$$

The corresponding free-surface Green's function $\tilde{G}(\boldsymbol{x},\boldsymbol{x}')$ is the solution to (4.2) with right-hand side equal to $\delta(\boldsymbol{x}-\boldsymbol{x}')$. It is equal to the unbounded Green's function $G(\boldsymbol{x},\boldsymbol{x}')$ for $n=3$ in (2.16) provided an equal-and-opposite image source term is added at the mirrored location $(x',y',-z')$ to ensure that the boundary condition $\tilde{G}(x,y,0,\boldsymbol{x}')=0$ is satisfied. The result is

$$\tilde{G}(\boldsymbol{x},\boldsymbol{x}')=G(\boldsymbol{x},x',y',z')-G(\boldsymbol{x},x',y',-z'), \tag{4.3}$$

which depends on the horizontal components of $\boldsymbol{x}-\boldsymbol{x}'$ and on both z and z'. Convolution with the specific source term in (4.2) yields

$$p=\int\tilde{G}(\boldsymbol{x},\boldsymbol{x}')\boldsymbol{R}\cdot\nabla'\,\delta(x')\delta(y')\delta(z'+h)\,\mathrm{d}V'=-\boldsymbol{R}\cdot\nabla'\,\tilde{G}(\boldsymbol{x},0,0,-h), \tag{4.4}$$

where the last term denotes the gradient of $\tilde{G}$ with respect to $\boldsymbol{x}'$ at the source location.

We consider separately the pressure field due to horizontal forces and that due to vertical forces. Let $\boldsymbol{R}_h=R_h\hat{\boldsymbol{x}}$ and $\boldsymbol{R}_v=R_v\hat{\boldsymbol{z}}$ denote the horizontal and vertical parts of $\boldsymbol{R}=\boldsymbol{R}_h+\boldsymbol{R}_v$ and similarly let the pressure be $p=p_h+p_v$. For horizontal forcing (4.4) can be simplified by using the symmetry $-\nabla'G=+\nabla G$ and the short-hand (2.21), which leads to

$$p_h=+R_h\frac{\partial}{\partial x}\tilde{G}(\boldsymbol{x},0,0,-h)=R_h\frac{\partial}{\partial x}(G_0(x,y,z+h)-G_0(x,y,z-h)). \tag{4.5}$$

For vertical forcing the z'-derivative of the Green's function $\tilde{G}$ leads to

$$p_v=R_v\frac{\partial}{\partial z}(G_0(x,y,z+h)+G_0(x,y,z-h)). \tag{4.6}$$

Specifically, in three dimensions

$$p_h = -\frac{R_h}{4\pi}\frac{\partial}{\partial x}\left\{\frac{1}{\sqrt{x^2+y^2+(z+h)^2}} - \frac{1}{\sqrt{x^2+y^2+(z-h)^2}}\right\} \tag{4.7}$$

and

$$p_v = -\frac{R_v}{4\pi}\frac{\partial}{\partial z}\left\{\frac{1}{\sqrt{x^2+y^2+(z+h)^2}} + \frac{1}{\sqrt{x^2+y^2+(z-h)^2}}\right\}. \tag{4.8}$$

It is important that p_h and p_v differ markedly in the far field $r \gg h$. The far-field form of p_h is computed from (4.7) by Taylor-expanding in h, which yields

$$p_h \approx -h\frac{3R_h}{2\pi}\frac{xz}{r^5}. \tag{4.9}$$

This decays rapidly as $O(r^{-3})$ and therefore the net momentum flux $\boldsymbol{\Phi} = 0$ as $\mathscr{D} \to \infty$. In other words, the impulsive fluid response to horizontal forcing in the presence of a free surface is entirely confined to fluid acceleration, i.e. $\boldsymbol{M}(0) = \boldsymbol{R}_h$ for sufficiently large control volumes $\mathscr{D}$. This holds without ambiguity for all shapes of $\mathscr{D}$.

On the other hand, p_v has a dipolar far-field form

$$p_v \approx 2\frac{R_v}{4\pi}\frac{z}{r^3}, \tag{4.10}$$

which does not depend on the forcing depth h. This pressure field is exactly twice the three-dimensional pressure due to impulsive forcing in an unbounded domain as computed in (2.22). Integrating p_v over a hemispheric control volume $\mathscr{D}$ in the lower half-plane thus yields the same result as before, namely $\boldsymbol{\Phi} = \boldsymbol{R}_v/3$. This result also depends on the shape of $\mathscr{D}$. In summary, we have obtained that for hemispherical control volumes

$$\boldsymbol{M}(0+) = \boldsymbol{R}_h + \tfrac{2}{3}\boldsymbol{R}_v \quad \text{and} \quad \boldsymbol{\Phi} = \tfrac{1}{3}\boldsymbol{R}_v \tag{4.11}$$

as $\mathscr{D} \to \infty$.

The differences in the fluid response to horizontal and vertical forcing can also be understood qualitatively by inspection of the image sources that were used in the construction of $\tilde{G}$. More precisely, the image sources can be thought of as arising from an image force field in the upper half-plane $z > 0$ that has the required equal-and-opposite divergence field when compared to the physical force field in $z < 0$; see figure 3(a). The impulsive pressure in $z < 0$ can then be thought of as arising from the combined image and physical force system in an unbounded fluid.

By inspection, the correct image force field has horizontal components that are sign-reversed compared to the horizontal components of the physical force field and vertical components that are identical. Therefore the integral over both the physical and the image force field has zero horizontal component and doubled vertical component. It is this integral which controls the far-field pressure field. This makes obvious why $p_h = O(r^{-3})$ whilst p_v has the dipolar, $O(r^{-2})$, form that is twice that for unbounded flow. These considerations also explain why the far field of p_h is proportional to h and vanishes as $h \to 0$. This is because $h \to 0$ corresponds to a coalescence of the opposing horizontal components of the image and physical force fields.

4.2. *Impulsive velocity field and flow adjustment*

The impulsive velocity field at $t = 0+$ is again given by (2.7), i.e. $\boldsymbol{u}(\boldsymbol{x}, 0+) = \boldsymbol{F} - \nabla p$. Of particular interest is the velocity at the free surface $z = 0$ because it determines the

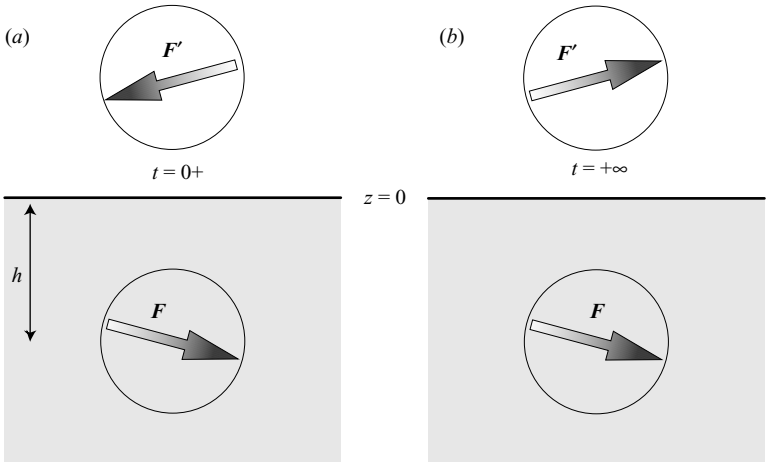

FIGURE 3. Image force system for computing the flow at $t=0+$ and $t=+\infty$ by using impulsive-forcing theory for an unbounded fluid. (*a*) For $t=0+$ the physical force $\boldsymbol{F}$ centred at $z=-h$ is paired with an image force $\boldsymbol{F}'$ centred at $z=h$ such that $\nabla\cdot\boldsymbol{F}$ is equal and opposite to $\nabla\cdot\boldsymbol{F}'$. This ensures $\tilde{p}=0$ at the flat interface $z=0$. (*b*) For $t=+\infty$ the image force has to be reversed to ensure $w=0$ at $z=0$.

generation of surface waves. The horizontal components u and v at $z=0$ are in fact zero because the pressure is horizontally homogeneous by the free-surface boundary condition. However, the vertical velocity w is not zero at the free surface. Specifically,

$$w=-\frac{\partial p}{\partial z}=-\frac{\partial p_h}{\partial z}-\frac{\partial p_v}{\partial z}\quad\text{at}\quad z=0, \tag{4.12}$$

and substitution of (4.7) and (4.8) yields the contributions

$$-\left.\frac{\partial p_h}{\partial z}\right|_{z=0}=\frac{3R_h}{2\pi}\frac{hx}{(x^2+y^2+h^2)^{5/2}}, \tag{4.13}$$

$$-\left.\frac{\partial p_v}{\partial z}\right|_{z=0}=-\frac{R_v}{2\pi}\frac{1}{(x^2+y^2+h^2)^{3/2}}+\frac{3R_v}{2\pi}\frac{h^2}{(x^2+y^2+h^2)^{5/2}}, \tag{4.14}$$

where $\boldsymbol{R}_h$ is aligned with the x-axis as before. Thus, horizontal forcing leads to a dipolar structure with rising motion ahead of the forcing region and sinking motion behind it. Vertical forcing leads to a monopolar axisymmetric structure that changes sign at horizontal distance $\sqrt{x^2+y^2}=\sqrt{2}h$ such that for negative R_v (i.e. downward forcing) there is sinking motion in a small inner region and rising motion elsewhere. In the presence of both horizontal and vertical forcing the far field w is dominated by the term with slowest decay, which is the monopolar term proportional to R_v.

The presence of non-zero w at the surface implies the impulsive generation of surface waves, which subsequently propagate away from the site of the forcing. Just as in the compressible case these waves can carry momentum out of a control volume $\mathscr{D}$ centred at the forcing site. The only difference is that surface waves are dispersive whereas sound waves are not. This raises the question of whether all waves will propagate away from the forcing site as $t\to\infty$. This will be the case if the group velocity for all wavenumbers is non-zero and this is indeed satisfied for surface waves under the influence of gravity and/or surface tension (see (4.21)). Thus, the flow can be expected to adjust to a steady balanced flow by the emission and propagation of unsteady surface waves. This steady flow is entirely controlled by the vorticity

distribution and it is therefore independent of the details of the waves, such as their dispersion relation.

The balanced flow can be computed directly by writing the velocity field explicitly as the sum

$$\boldsymbol{u} = \boldsymbol{u}_b + \boldsymbol{u}_w \tag{4.15}$$

of a balanced and a wave part such that $\nabla \times \boldsymbol{u}_b = \nabla \times \boldsymbol{F}$ and $\nabla \times \boldsymbol{u}_w = 0$. In addition, the boundary condition for the balanced flow is $w_b = 0$ at $z = 0$. With this definition, plus suitable decay conditions at infinity, the balanced flow is a well-defined steady solution of the linear equations. As before, $\boldsymbol{u}_b$ can be viewed as the least-square projection of $\boldsymbol{F}$ onto non-divergent vector fields subject to the additional constraint $w_b = 0$ at $z = 0$. For a localized force field the balanced flow is essentially that of a vortex ring centred at the forcing position and aligned with $\boldsymbol{R}$.

Computing directly the net momentum transported away by the surface waves is more complicated than in the compressible case because of wave dispersion. However, this complication can be side-stepped by considering a thought experiment in which the balanced flow itself is set up impulsively and therefore its momentum can be computed directly by the methods of § 2.4. Since the momentum of a given flow does not depend on how the flow has been set up this establishes the momentum of the balanced flow.

To this end the boundary condition at $z = 0$ is changed from free-surface type (i.e. $\tilde{p} = 0$) to rigid-lid type (i.e. $w = 0$). For horizontal forcing this is equivalent to an image force in the upper half-plane that points in the same direction as $\boldsymbol{F}$, see figure 3(*b*). This makes clear that the impulsive pressure in the far field is twice that of a horizontal $\boldsymbol{F}$ alone in an unbounded domain and therefore the net flux of horizontal momentum across a large hemispheric control volume is equal to the usual $\boldsymbol{R}_h/3$ in three dimensions. This construction shows that the momentum of the balanced flow due to horizontal forcing has the value $2\boldsymbol{R}_h/3$ in relation to a large hemispherical control volume.

To compute the balanced response to vertical forcing we place a solid wall at $z = 0$ during the impulsive forcing; see figure 3(*b*) for the appropriate image force system in this case. By continuity it is then kinematically impossible to have any vertical movement of the centre of mass of the incompressible fluid in $z < 0$, and this implies that the momentum of the balanced flow due to vertical forcing must be precisely zero. It can be checked by direct computation (i.e. by inversion of the vorticity field) that this kinematic argument is correct and holds without ambiguity as $\mathscr{D} \to \infty$.

This explains the peculiar result that $\boldsymbol{M}(+\infty) = 0$ in this case even though there is a downward-moving vortex ring. Physically, the upward return flow outside the vortex ring precisely cancels the momentum inside the vortex ring in this configuration. This contrasts with the initial value of Kelvin's impulse, which is $\boldsymbol{I}(0+) = \boldsymbol{R}$ by construction. Note, however, that $\boldsymbol{I}$ is not constant for bounded flow domains. As in § 2.5, this illustrates that neither $\boldsymbol{M}(0+)$ nor $\boldsymbol{M}(+\infty)$ are related to Kelvin's impulse $\boldsymbol{I}$ in a simple way.

In summary, we have obtained that

$$\boldsymbol{M}(0+) = \boldsymbol{R}_h + \tfrac{2}{3}\boldsymbol{R}_v \quad \text{and} \quad \boldsymbol{M}(+\infty) = \tfrac{2}{3}\boldsymbol{R}_h. \tag{4.16}$$

During the adjustment process the surface waves must carry away 1/3 of the horizontal momentum $\boldsymbol{R}_h$ and 2/3 of the vertical momentum $\boldsymbol{R}_v$. (In the two-dimensional version of (4.16) the 2/3 is replaced by 1/2.) The remaining 1/3 of $\boldsymbol{R}_v$ is carried away by the impulsive far-field pressure flux at $t = 0+$ (cf. (4.10)). It should

be noted that the flow adjustment due to surface wave propagation occurs with finite speed and that therefore the convergence of $\boldsymbol{M}(t)$ to $\boldsymbol{M}(+\infty)$ is non-uniform with respect to the radius of the control volume. In other words, larger control volumes require waiting for longer times before $\boldsymbol{M}(t) \approx \boldsymbol{M}(+\infty)$ because the wave front moves with a finite speed and it is the crossing of $\partial\mathscr{D}$ by the wave front that marks the adjustment in $\boldsymbol{M}$.

For oblique recoil forces (4.16) indicates that both $\boldsymbol{M}(0+)$ and $\boldsymbol{M}(+\infty)$ make a shallower angle with the horizontal than $\boldsymbol{R}$. Regarding magnitudes, if the impulsive force $\boldsymbol{R}$ makes an angle θ with the horizontal then

$$|\boldsymbol{M}(0+)| = |\boldsymbol{R}|\sqrt{1 - \tfrac{5}{9}\sin^2\theta} \quad \text{and} \quad |\boldsymbol{M}(+\infty)| = |\boldsymbol{R}|\tfrac{2}{3}\cos\theta. \tag{4.17}$$

4.3. *Dynamics of surface waves*

For completeness, how the detailed surface-wave dynamics during the adjustment process can be computed is briefly described. This is useful for flow observations and for the experimental water strider considerations discussed in § 5.3.

The irrotational velocity component related to the waves is governed by the vertical surface undulation $\zeta(x, y, t)$ defined such that $\zeta = 0$ corresponds to a flat surface. The initial-value problem for the surface waves after impulsive forcing can be written in terms of the already computed vertical velocity at the surface as

$$\zeta(x, y, 0) = 0 \quad \text{and} \quad \zeta_t(x, y, 0) = (4.13) + (4.14). \tag{4.18}$$

The wave solution in time is computed using a two-dimensional Fourier transform for ζ such that

$$\zeta(x, y, t) = \frac{1}{(2\pi)^2}\int\int \hat{\zeta}(k, l, t)\exp(\mathrm{i}[kx + ly])\,\mathrm{d}k\mathrm{d}l. \tag{4.19}$$

For a plane wave solution $\zeta \propto \exp(\mathrm{i}[kx + ly - \omega t])$ with given wavenumber vector $\boldsymbol{k} = (k, l)$ the frequency $\omega(\boldsymbol{k})$ is determined by the dispersion relation. For surface waves there are two branches $\pm\omega(\boldsymbol{k})$, where $\omega(\boldsymbol{k}) = \omega(-\boldsymbol{k}) \geqslant 0$ is the positive branch of the dispersion relation. This choice is convenient because for surface waves the dispersion relation depends only on $\kappa = |\boldsymbol{k}|$ and thus using the positive dispersion relation $\omega(\kappa) \geqslant 0$ is natural. Using the reality condition the general solution for $\hat{\zeta}$ is

$$\hat{\zeta}(\boldsymbol{k}, t) = \hat{\zeta}(\boldsymbol{k}, 0)\cos\omega t + \hat{\zeta}_t(\boldsymbol{k}, 0)\frac{1}{\omega}\sin\omega t. \tag{4.20}$$

Specifically, for deep-water waves with surface tension the positive dispersion relation is

$$\omega(\kappa) = +\sqrt{g\kappa + \gamma\kappa^3} \quad \text{and therefore} \quad \frac{\mathrm{d}\omega}{\mathrm{d}\kappa} = \frac{1}{2}\frac{g + 3\gamma\kappa^2}{\sqrt{g\kappa + \gamma\kappa^3}}, \tag{4.21}$$

where g is acceleration due to gravity and γ is the surface tension divided by the water density. As noted before, this dispersion relation has the required non-zero group-velocity property for all wavenumbers.

5. Water strider locomotion

5.1. *Observations and theory*

The water strider is a small insect that can stand and move on water by exploiting the surface tension of the air–water interface. The typical insect has a core body

size of about 1 cm and supports its weight on thin long hydrophobic legs that bend the water surface. It propels itself forward by a rapid sculling motion of its central pair of legs. The static force balance of a water strider standing on water is very well understood (e.g. Keller 1998), but the dynamical mechanism of water strider locomotion has proven much harder to grasp (see review and references in Bush & Hu 2006).

Casual observation of water strider movement invariably shows the presence of small-scale capillary waves excited by the rapid sculling motion of the insect's legs. The presence of these waves, which are easily detected by the naked eye, together with the fact that the water strider does not pierce the surface during its leg stroke, has led to the early hypothesis that the recoil on the strider may be primarily due to momentum transferred to the surface waves by the leg stroke (e.g. Denny 1993). For instance, using irrotational flow theory and wave-makers that move at constant speed, this momentum transfer has been computed for surface pressure disturbances and for partially submerged bodies by Raphael & de Gennes (1996) and Sun & Keller (2001), respectively.

Observations by the naked eye can be vastly improved by the use of flow visualization methods and Hu *et al.* (2003) applied such methods to the study of water-walking insects. These experiments clearly demonstrated the presence of subsurface vortex dipoles, which are shed by the sculling legs of the insect seemingly in the same fashion as vortices are shed by rowing oars. (Note that Suter *et al.* (1997) first presented the important physical picture of water-walking insects using their menisci as blades.) Furthermore, the momentum of the fluid trapped in these vortices was estimated from the laboratory data and found to be comparable to the insect recoil, which led to the alternative hypothesis that the insect recoil may be primarily due to momentum transferred into these vortices. The appearance of these vortices is remarkable in itself because the insect's legs do not pierce the surface as rowing oars do. Without the broken surface there is no obvious viscous boundary layer that could shed vorticity at the high Reynolds number of the leg stroke (which was estimated to be about 10^3 based on the leg contact area and a maximum leg speed of about $100\,\mathrm{cm\,s^{-1}}$). The answer appears to be that the fine hairs on the hydrophobic legs sufficiently adhere to the water that, effectively, a small contact surface area is materially dragged along with the sculling legs, and this imposed no-slip motion on the surface apparently generates the viscous boundary layer need for the vorticity shedding.

In principle, the quantitative partitioning of recoil momentum into waves and vortices can be determined experimentally. For instance, as noted in § 2.5 and § 4.2, the horizontal momentum in the vortices can be estimated either from measurements of the Kelvin impulse derived from the vorticity distribution (cf. Drucker & Lauder 1999) or from visualizations of the trapped fluid in the vortices (cf. Hu *et al.* 2003). On the other hand, it is more difficult to estimate the momentum of the waves. This difficulty is compounded by the impulsive and transient nature of the leg stroke, which rules out using the classical theory of slowly varying wavetrains. Indeed, such wavetrains would arise only from the action of a wave source that undergoes stationary oscillations rather than impulsive motion; this means a paddling leg rather than a sculling one, and a mode of propulsion similar to that of the model boat in the experiment described in Longuet-Higgins (1977).

Not surprisingly, then, attempts to use the inapplicable slowly varying wavetrain theory for water strider locomotion have quickly led to difficulties. For instance, matching the observed leg speed to the phase speed of an excited wave mode

permitted by the dispersion relation (4.21) is impossible if the leg speed falls below the minimum phase speed $(4g\gamma)^{1/4} \approx 23\,\mathrm{cm\,s^{-1}}$. Apparently, this is the case for baby water striders, and therefore these baby insects cannot produce wave drag according to slowly varying wavetrain theory, as was pointed out by Denny (1993).

Similarly, the leading-order recoil force on an oscillatory wave source computed from wavetrain theory is necessarily quadratic in wave amplitude because the linear forces cancel over one wave period. It has been shown in Hu *et al.* (2003) that applying the quadratic wavetrain force formula to the experimental wave data yields a recoil force that is much smaller than the observed water strider recoil. However, the recoil force due to impulsive forcing is linear in the wave amplitude, and this is much bigger than a quadratic force for small wave amplitude. Indeed, the square root of the quadratic recoil force estimate in Hu *et al.* (2003) is of the same order of magnitude as the observed recoil. This observation motivated the present study in which impulsive-forcing theory is applied to the momentum exchange during the leg stroke.

This is pursued in the next section and the net result is a synthesis between the wave and vortex momentum hypotheses: both types of fluid motion contribute significantly to the insect's horizontal recoil, with shares 1/3 and 2/3, respectively.

5.2. *Insect recoil modelled by impulsive forcing theory*

At rest, the static insect leg bends the water surface downwards such that a meniscus of approximate depth $h = 0.1$ cm is formed that supports the weight of the insect. During the leg stroke the leg moves rapidly and horizontal momentum is exchanged between the water and the insect, manifested in the insect's recoil on the one hand and fluid waves and vortices on the other. Specifically, the insect exerts a horizontal force ρR_h on the fluid and the insect's recoil is therefore $-\rho R_h$. A full mechanical description of the impulsive leg stroke involves a three-dimensional time-dependent fluid–structure interaction problem with a free boundary and at high Reynolds number. At present such a problem cannot be solved either analytically or numerically and hence only idealized versions of the leg stroke can be considered for analysis.

Here a severe idealization is considered in which the leg stroke is modelled by an impulsive force localized at the location of the leg and acting on an undisturbed fluid with an initially flat surface at $z = 0$. That is, the insect leg as well as its static meniscus have been entirely removed from consideration. The argument for this modelling approach is that the far-field fluid response should be dominated by the net recoil force exerted on the fluid and not by the details of the force distribution. It is the far-field response, i.e. the fluid response at distances much bigger than h, that can be measured in an experiment and we seek to relate this to the insect recoil. Arguably, if we excise the true leg–water interaction region and replace it by a region of uniform fluid subject to a net force then we will not change the asymptotic fluid response at distances large compared to the forcing region.

It is noteworthy that surface tension and nonlinear effects might be crucially important for the intricate workings of the true leg–water interaction region, for instance strong surface tension may be necessary to ensure that the leg does not break through the water surface. However, they do not affect the large-scale fluid response during the leg stroke at distances sufficiently far away from the forcing region.

This asymptotic fluid response in terms of vortices and surface waves is computed from the impulsive force theory described in §4.1. It depends only on the net momentum transfer per unit mass R_h and on the forcing depth h, which means

that these quantities can be related to measurable properties of the wave and vortex response.

The present model neglects one obvious physical effect that may affect observations, namely the monopolar surface waves generated by lifting the insect's leg from its static position and releasing the meniscus. If desired, this effect could be added to the surface wave pattern by using the theoretical shape of the meniscus as a further contribution to the initial-value problem for the free surface. This could be important for very accurate wave measurements, not least because the monopolar waves exhibit slower decay with radius than dipolar waves (cf. (4.14)). However, it is clear that these monopolar waves do not carry any horizontal momentum and thus their inclusion would not affect the estimate for R_h. Similarly, within linear theory it would be possible to consider an arbitrary surface shape at $t=0$ as this would only add another homogeneous free-wave solution to the problem.

5.3. *Stroke modelling details*

The leg sits at a typical rest depth $h=0.1\,\mathrm{cm}$ inside the static meniscus just before the stroke. It is reasonable to use this value of h for the depth of the impulsive forcing as well. The physical parameters (in cgs units) are gravity $g=981\mathrm{cm\,s^{-2}}$, air–water surface tension divided by water density $\gamma=74\,\mathrm{cm^3\,s^{-2}}$, and the kinematic viscosity of water $\nu=0.01\,\mathrm{cm^2\,s^{-1}}$. The viscosity leads to dissipation of kinetic energy and hence to damping of plane surface waves with exponential rate $2\nu\kappa^2$, where $\kappa=\sqrt{k^2+l^2}$ is the magnitude of the horizontal wavenumber vector $\boldsymbol{k}=(k,l)$ (e.g Lamb 1932, p. 625). For weakly dissipating plane waves (i.e. waves whose damping rate is small compared to their frequency) the only modification in the solution to the non-dissipative initial-value problem described in § 4.3 is to multiply the undamped spectral solution $\hat{\zeta}(\boldsymbol{k},t)$ by the decay factor $\exp(-2\nu\kappa^2 t)$. This is sufficient for the problem at hand. Roughly speaking, the surface wave evolution occurs over the time scale of a few hundredths of second and over this short time scale viscous dissipation acts significantly on waves with scales of a millimetre or less.

The initial condition for the surface waves is an undisturbed surface and a vertical surface velocity given by (4.13), which yields

$$\zeta(x,y,0)=0 \quad \text{and} \quad \zeta_t(x,y,0)=\frac{3R_h}{2\pi}\frac{hx}{(x^2+y^2+h^2)^{5/2}} \tag{5.1}$$

if the leg stroke direction is aligned with the x-axis. Here R_h is the net momentum transfer per unit mass into the fluid. The insect recoil is therefore $-\rho R_h$, where ρ is the density of water, which is unity in cgs units.

The initial-value problem is solved numerically using a doubly periodic square domain with side length 6 cm and up to 512 spectral modes, which is sufficient to compute quantities such as the maximum surface elevation with 1 %. A typical image of the surface elevation $\zeta(\boldsymbol{x},t)$ is illustrated in figure 4. The dominant structure is an expanding dipolar surface wave with raised surface in the direction of forcing. The horizontal scale of the dipole is much bigger than h and the dipole is preceded by small-scale ripples, which have appreciable magnitude on the scale of h. For the time shown, these small-scale ripples have been significantly affected by the viscous dissipation but the dipole has not. The overall dynamics of the wave pattern is dominated by surface tension and gravity plays a lesser role. This is important for the maximum wave height discussed next.

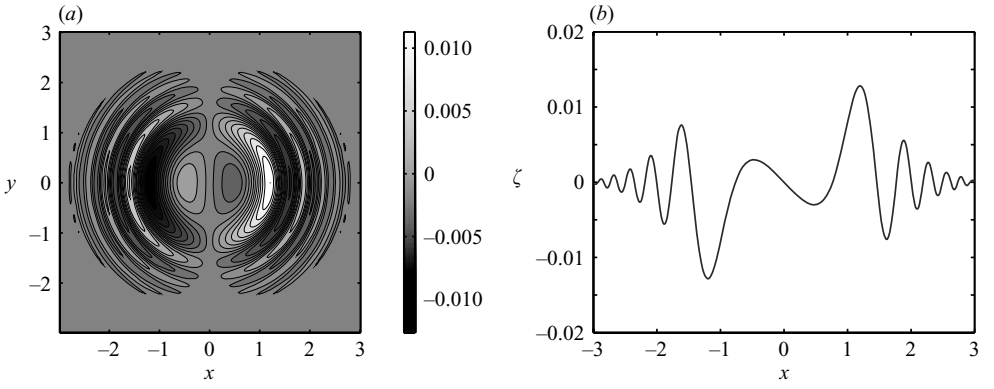

FIGURE 4. Numerical solution of deep-water system with surface tension subject to impulsive forcing using the initial conditions (5.1). The parameters are $R_h = 0.5\,\mathrm{cm}^4\,\mathrm{s}^{-1}$ and $h = 0.1$ cm. (*a*) Surface elevation ζ at time $t = 0.04$ in cgs units, showing large-scale dipolar structure and small-scale ripples that act as forerunners. (*b*) Elevation on $y = 0$ at the same time (cf. figure 2).

5.4. *Scaling for maximum wave height*

The maximum surface elevation $\zeta_* = 0.06$ cm is attained at the leading dipole at the very early time $t_* = 0.0027$ s and dimensional analysis gives an interesting scaling for both ζ_* and t_*. The elevation ζ_* is explicitly linear in R_h and otherwise it is a certain function of h, g, γ, and viscosity ν. Dimensional analysis then implies that

$$\frac{\zeta_*}{h} = \frac{R_h}{\sqrt{\gamma h^5}}\, f\left(\frac{gh^2}{\gamma}, \frac{\nu}{\sqrt{\gamma h}}\right), \tag{5.2}$$

where $f(\cdot, \cdot)$ is a non-dimensional function of the non-dimensional gravity and viscosity as indicated. For the chosen h the non-dimensional gravity is about 0.1, which indicates the dominance of surface tension, and the non-dimensional viscosity is about 0.004, which indicates that viscous effects are irrelevant for ζ_*. This suggests a scaling law based on replacing $f(\cdot, \cdot)$ by a constant approximating $f(0, 0)$, i.e.

$$\zeta_* \propto \frac{R_h}{\sqrt{\gamma h^3}} = 0.032\,\frac{R_h}{\sqrt{\gamma h^3}} \quad \text{and also} \quad t_* = 0.74\sqrt{\frac{h^3}{\gamma}} \tag{5.3}$$

by repeating the argument for t_*. The proportionality factors have been determined from the numerical simulation.

Interestingly, (5.3) implies that for fixed R_h the maximal elevation $\zeta_* \propto h^{-3/2}$, and therefore ζ_* increases rapidly with decreasing forcing depth h: a shallower stroke of equal force produces a much bigger splash.

5.5. *Vortex flow*

By definition, the balanced vortex flow $\boldsymbol{u}_b$ satisfies the rigid-lid boundary condition $w_b = 0$ at $z = 0$ and has vorticity

$$\nabla \times \boldsymbol{u}_b = \nabla \times \boldsymbol{F} = \nabla \times (\widehat{\boldsymbol{x}} R_h\, \delta(x)\delta(y)\delta(z + h)), \tag{5.4}$$

which corresponds to an infinitesimal vortex ring aligned with the x-axis and centred at $x = y = 0$ and $z = -h$. According to linear inviscid theory, the flow adjusts to this steady balanced flow by the wave emission such that $\boldsymbol{u}(\boldsymbol{x}, t) \to \boldsymbol{u}_b(\boldsymbol{x})$ as $t \to \infty$ for fixed $\boldsymbol{x}$. We first consider the structure of the inviscid balanced flow by using $\boldsymbol{u}_b = \boldsymbol{F} + \nabla\phi$

and solving for the three-dimensional potential ϕ such that

$$\nabla^2\phi = -\nabla\cdot\boldsymbol{F} \quad \text{subject to} \quad \phi_z = 0 \quad \text{at} \quad z = 0 \quad \text{and} \quad \nabla\phi \to 0 \quad \text{as} \quad r \to \infty. \tag{5.5}$$

The Green's function for the rigid-lid boundary condition is (cf. (2.21))

$$\bar{G}(\boldsymbol{x}, \boldsymbol{x}') = G_0(x - x', y - y', z - z') + G_0(x - x', y - y', z + z') \tag{5.6}$$

and this yields

$$\phi(x, y, z) = -\frac{R_h}{4\pi}\left\{\frac{x}{(x^2 + y^2 + (z + h)^2)^{3/2}} + \frac{x}{(x^2 + y^2 + (z - h)^2)^{3/2}}\right\}. \tag{5.7}$$

Specifically, at the free surface $w_b = 0$ and the horizontal velocities follow from the surface potential

$$\phi(x, y, 0) = -\frac{R_h}{2\pi}\frac{x}{(x^2 + y^2 + h^2)^{3/2}}. \tag{5.8}$$

This balanced surface flow has some surprising features. For instance, on the centreline $y = 0$ there is a backward flow $u_b < 0$ if $|x| \ll h$ and a forward flow $u_b > 0$ if $|x| \gg h$. Also, the flow is irrotational in the free surface. Both these features are consistent with the three-dimensional rolling motion induced by an infinitesimal vortex ring submerged at depth h. Despite this consistency, however, such a vortex flow structure is not observed in experiments.

This is because the vortex flow is observable for a fraction of a second and this is a long enough time interval that nonlinear and viscous effects must be taken into account. Indeed, in nonlinear viscous theory the vortex ring self-advects nonlinearly in the x-direction whilst its vorticity and velocity structure rapidly diffuses outward. These effects are easily observable in the water strider experiments in Hu *et al.* (2003). Nonlinearity cannot be treated here, but viscous diffusion is easily incorporated into the balanced flow evolution by letting $\boldsymbol{u}_b$ diffuse according to

$$\frac{\partial \boldsymbol{u}_b}{\partial t} = \nu\nabla^2\boldsymbol{u}_b \quad \text{and} \quad \left(\frac{\partial u_b}{\partial z}, \frac{\partial v_b}{\partial z}, w_b\right) = 0 \quad \text{at} \quad z = 0. \tag{5.9}$$

These boundary conditions correspond to a 'slippery' rigid lid that does not support tangential stresses. Thus, during a fraction of a second $\boldsymbol{u}_b$ rapidly diffuses outwards from $z = -h$ and this quickly changes the horizontal flow in the free surface. The evolving $\boldsymbol{u}_b$ has a three-dimensional structure but in the surface $z = 0$ it takes the simple form of a vortex pair together with a divergent source–sink flow.

This is illustrated in figure 5, where the balanced flow in the surface $z = 0$ at time $t = 0.5$ s is visualized using a Helmholtz decomposition for the horizontal velocities such that $(u_b, v_b) = (\phi_x - \psi_y, \phi_y + \psi_x)$. This decaying surface flow resembles a cross-section of Hill's hemispherical vortex and the trapped fluid momentum can be estimated on this basis as in Hu *et al.* (2003).

6. Concluding remarks

The results in this paper follow from the assumptions that the fluid is forced for a short time and in a compact region. For instance, it is the *rapidity* of impulsive fluid forcing that allows the use of linear theory. The same rapidity also implies that any linear fluid dynamics concerning material displacements, such as surface waves, can be neglected during the impulsive forcing. A similar finding occurred in the asymptotic analysis of Sun & Keller (2001) with regard to the contact region between a rapidly

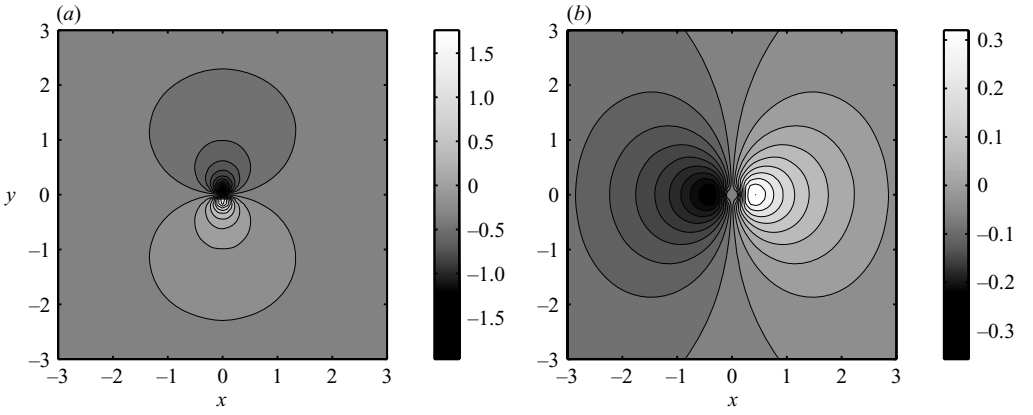

FIGURE 5. A numerical solution to (5.9) is evaluated for the horizontal balanced flow in the free surface $z = 0$ at time $t = 0.5$ s. The physical parameters are as before. Displayed are the stream function ψ and velocity potential ϕ such that $(u_b, v_b) = (\phi_x - \psi_y, \phi_y + \psi_x)$ at $z = 0$. (*a*) The stream function ψ exhibits a typical vortex-pair structure that corresponds to vortex propagation to the right. (*b*) The velocity potential ϕ indicates convergence and hence sinking motion just below the surface in $x > 0$ and a compensating divergence region and rising motion in $x < 0$.

moving partly submerged body and the fluid underneath, where it was found that neither gravity nor surface tension played a role in the contact region.

The *smallness* of the forcing region compared to the size of the generated waves and vortices is also important for the practical relevance of the highly idealized leg-stroke model in § 5.3. For instance, the initial conditions for the surface waves are (5.1) and they are much broader than the meniscus depth $h = 0.1$ cm that is used as the forcing depth. The same applies to the vortex motion depicted in figure 5. It seems plausible that the intricate and nonlinear details of the true fluid–structure interactions during the leg stroke would add further small-scale details to the fluid motion but that they would not change large-scale results such as the partitioning of momentum between waves and vortices.

In this paper, the horizontal wave and vortex momenta have been computed using a deep-water assumption. Presumably, an extension to water of finite depth would yield a smooth transition between the three-dimensional result $(1/3, 2/3)$ and the two-dimensional result $(1/2, 1/2)$ as the water depth becomes small. Indeed, the latter must apply in the shallow water limit by using the analogy between shallow water and compressible fluid flow.

Another interesting question is how the partitioning of momentum between waves and vortices could be affected by nonlinear effects after the leg stroke. Broadly speaking, global momentum conservation implies that nonlinear interactions within a distribution of irrotational surface waves cannot change the net momentum associated with the waves. Similarly, nonlinear interactions within the vortical balanced dynamics conserve vortex momentum. Thus, the only way to exchange momentum is by nonlinear interactions between the waves and the vortices. This kind of interaction is certainly possible (e.g. Bühler & McIntyre 2003, 2005) but is neglected by the linear theory presented in this paper. A quantitative argument for this neglect is to note that the dispersive surface waves very quickly propagate away from the region of vortical flow, which suggests that there is very little time for systematic nonlinear interactions between waves and vortices.

Another question concerns the utility of the waves and vortices for the biolocomotion of water-walking insects. This paper suggests that both waves and vortices are inevitable and that their respective strength as measured by the horizontal momentum is 1/3 to 2/3. However, a more useful measure for the insect might be the energy in these motions at fixed recoil momentum. Arguably, the insect would like to minimize that energy. Unlike the momentum, the energy is sensitive to the higher moments of the forcing field and it would be interesting to know the force-field structure that creates the fluid response with minimal wave and vortex energy under the constraints of fixed compact support and fixed net integral.

I would like to thank J. W. M. Bush and D. L. Hu for the very interesting discussions of their experimental work on water walkers that motivated this theoretical work. The non-uniqueness of the global momentum budget for incompressible flows was first pointed out to me a long time ago by M. E. McIntyre, and it is a pleasure to acknowledge many stimulating discussions on this and related topics ever since. D. G. Andrews kindly provided me with a reference to (and a copy of) the important work of Theodorsen (1941). The comments of several referees significantly improved this paper. Financial support for the wave–vortex theoretical aspects of this work under NSF grant OCE-0324934 is gratefully acknowledged. This paper was written up largely at the NSF-sponsored 2005 summer program in Geophysical Fluid Dynamics hosted by the Woods Hole Oceanographic Institution (USA), and I would like to thank the 2005 GFD directors for their support.

REFERENCES

Batchelor, G. K. 1967 *An Introduction to Fluid Dynamics*. Cambridge University Press.

Bretherton, F. P. 1969 On the mean motion induced by internal gravity waves. *J. Fluid Mech.* **36**, 785–803.

Bühler, O. & McIntyre, M. E. 2003 Remote recoil: a new wave–mean interaction effect. *J. Fluid Mech.* **492**, 207–230.

Bühler, O. & McIntyre, M. E. 2005 Wave capture and wave–vortex duality. *J. Fluid Mech.* **534**, 67–95.

Bush, J. W. M. & Hu, D. L. 2006 Walking on water: biolocomotion at the interface. *Annu. Rev. Fluid Mech.* **38**, 339–369.

Denny, M. W. 1993 *Air and Water: The Biology and Physics of Life's Media*. Princeton University Press.

Drucker, E. G. & Lauder, G. V. 1999 Locomotor forces on a swimming fish: three-dimensional vortex wake dynamics quantified using digital particle image velocimetry. *J. Expl Biol.* **202**, 2393–2412.

Hu, D. L., Chan, B. & Bush, J. W. M. 2003 The hydrodynamics of water strider locomotion. *Nature* **424**, 663–666.

Keller, J. B. 1998 Surface tension force on a partly submerged body. *Phys. Fluids* **10**, 3009–3010.

Lamb, H. 1932 *Hydrodynamics,* 6th edn. Cambridge University Press.

Longuet-Higgins, M. S. 1977 The mean forces exerted by waves on floating or submerged bodies with applications to sand bars and wave power machines. *Proc. R. Soc. Lond.* A **352**, 463–480.

McIntyre, M. E. 1981 On the 'wave momentum' myth. *J. Fluid Mech.* **106**, 331–347.

Raphael, E. & de Gennes, P.-G. 1996 Capillary gravity waves caused by a moving disturbance; wave resistance. *Phys. Rev.* E **53**, 3448.

Sun, S.-M. & Keller, J. B. 2001 Capillary-gravity wave drag. *Phys. Fluids* **13**, 2146–2151.

Suter, R., Rosenberg, R., Loeb, S., Wildman, H. & Long, J. J. 1997 Locomotion on the water surface: propulsive mechanisms of the fisher spider dolomedes triton. *J. Expl Biol.* **200**, 2523–2538.

Theodorsen, T. 1941 Impulse and momentum in an infinite fluid. In *Von Karman Anniversary Volume*, pp. 49–57. Caltech.